

Characterization of electron and phonon transports in Bi-doped CaMnO_3 for thermoelectric applications

E. Suprayoga,¹ W. B. K. Putri,¹ K. Singsoog,² S. Paengson,^{2,3} M. Y. Hanna,¹ A. R. T. Nugraha,¹ D. R. Munazat,⁴ B. Kurniawan,⁴ M. Nurhuda,⁵ T. Seetawan,^{2,3,*} and E. H. Hasdeo^{1,6,†}

¹*Research Center for Physics, Indonesian Institute of Sciences (LIPI), Tangerang Selatan 15314, Indonesia*

²*Center of Excellence on Alternative Energy, Research and Development Institution, Sakon Nakhon Rajabhat University, Sakon Nakhon 47000, Thailand*

³*Program of Physics, Faculty of Science and Technology,*

Sakon Nakhon Rajabhat University, Sakon Nakhon 47000, Thailand

⁴*Department of Physics, University of Indonesia, Depok 16424, Indonesia*

⁵*Department of Physics, Brawijaya University, Malang, 65145, Indonesia*

⁶*Physics and Materials Science Research Unit, University of Luxembourg, L-1511 Luxembourg*

(Dated: January 24, 2020)

Electron and phonon transports in CaMnO_3 and its Bi-doped counterpart, $\text{Bi}_{0.03}\text{Ca}_{0.97}\text{MnO}_3$, are investigated by thermoelectric transport measurements, Raman spectroscopy, and first-principles calculations. In particular, we focus on CaMnO_3 and $\text{Bi}_{0.03}\text{Ca}_{0.97}\text{MnO}_3$'s electronic structures, temperature-dependent electron and phonon lifetimes, and their sound velocities. We find that the anti-ferromagnetic insulator CaMnO_3 breaks the Wiedemann-Franz (WF) law with the Lorenz number reaching four times that of ordinary metals at room temperature. Bismuth doping reduces both the electrical resistivity and the Seebeck coefficient of CaMnO_3 , thus it recovers the WF law behavior. Raman spectroscopy confirms that $\text{Bi}_{0.03}\text{Ca}_{0.97}\text{MnO}_3$ has a lower Debye frequency as well as a shorter phonon lifetime. As a result, $\text{Bi}_{0.03}\text{Ca}_{0.97}\text{MnO}_3$ exhibits superior thermoelectric properties over the pristine CaMnO_3 due to the lower thermal conductivity and electronic resistivity.

I. INTRODUCTION

Perovskite oxides attract a lot of interests in the last decades due to their rich physical properties [1–3]. Strongly-correlated electrons originating from transition-metal atoms give rise to various types of ground states, such as anti-ferromagnetic insulators [4, 5], ferromagnetic metals [6] and even high- T_c superconductors [7]. These strongly-correlated perovskite oxides, in particular, can be applied in sensor technology utilizing their piezoelectric and large magnetoresistance [4], as well as to be used in energy harvesting technology, for example in solar cells and thermoelectric (TE) devices [8–11].

TE materials are a class of materials that can convert heat into electricity [12, 13]. Efficient TE materials should be thermally inert while electrically conducting at the same time. These requirements give researchers a challenge in designing TE materials because the electrons that are transporting charges in conventional metals are also carrying heat. According to the Wiedemann-Franz (WF) law, the ratio of electron thermal conductivity κ_e with respect to electrical conductivity σ is proportional to temperature [14] and thus a possible way to improve the TE efficiency is by breaking the WF law. The breaking of the WF law might be realized, for example, through the introduction of strongly-correlated Coulomb interactions [15–17].

The perovskite oxides are considered strongly-correlated electronic systems. In this regard, we propose

that one of the simplest perovskite oxides CaMnO_3 (or "CMO"), with a proper doping, could be a potential candidate for non-toxic and easily prepared TE materials. CMO is structurally stable even at temperature above 900°C, thus it is suitable for high-temperature TE materials [18]. At low temperature, CMO behaves as an insulator with anti-ferromagnetic ordering that originates from the Mott-like correlation [9, 19]. At higher temperatures, its electrical conductivity increases, hence allowing better TE performance. When doped with Bi into the Ca site, double-exchange interaction between two dissimilar Mn ions mediated by oxygen delocalizes electrons permitting metal ferromagnetic ground states [20]. It is important to note that, while the electronic contribution to the transport properties has been much understood, the phonon contribution to the thermal conductivity and the role of Bi doping to the phonon transport in CMO remain subtle.

In this work, we characterize electron and phonon transports in CMO and Bi-doped CMO (abbreviated as "BCMO") using TE transport measurements. We choose $\text{Bi}_{0.03}\text{Ca}_{0.97}\text{MnO}_3$ as the BCMO in the present study due to our expectation that this particular compound gives the best TE performance among various compositions of BCMO [11]. The Seebeck coefficients, electrical resistivities, and thermal conductivities are measurable quantities from the experiments that can be compared with first-principles calculations. By calculating the electronic structure and phonon energies of the materials (and comparing with the experimental results), it is possible to gain important quantities that determine transport properties of materials, such as the chemical potential, electron lifetime, phonon lifetime, the phonon Debye temper-

* t.seetawan@snru.ac.th

† eddw001@lipi.go.id

atures, and sound velocities. We also introduce Raman spectroscopy to better understand the role of Bi doping in the phonon transport.

Our TE measurements show that CMO has a reasonably high Seebeck coefficient of about $300\mu\text{V/K}$ at room temperature and it is even possible to optimize the Seebeck coefficient up to five times if the chemical potential is correctly tuned (at the band edge). Upon Bi doping, the electrical resistivity reduces by 10 times and the Seebeck coefficient reduces by 2 times, hence making a sizeable improvement in the power factor. Additionally, the presence of Bi doping adds more phonon scattering path via anharmonicity and increases atomic average mass. As a result, the sound velocity is reduced. This effect can be seen in the Raman spectra and is responsible for the decrease in thermal conductivity and for the enhancement of TE figure of merit. Other notable phenomenon is the breakdown of WF law in CMO with Lorenz number reaching four times of L_0 stemming from strongly correlated nature of electrons in CMO. Upon Bi-doping this Lorenz number recovers that of ordinary metals.

This paper is organized as follows. Experimental and theoretical methods are presented in Secs. II and III, respectively. Geometrical structure of CMO is confirmed via X-ray diffraction, as discussed in Sec. IV A. Electronic transport properties of CMO and BCMO are presented in Sec. IV B and IV C, respectively. The phonon transport including Raman spectroscopy and thermal conductivity are presented in Sec. IV D. Finally, conclusions are given in Sec. V.

II. EXPERIMENTAL METHODS

For characterization of the TE properties, the CMO and BCMO materials were synthesized by solid state reaction and hot press methods. The raw materials including CaCO_3 (QReC, $\geq 99\%$), MnO_2 (Fisher Scientific, $\geq 99.99\%$) and Bi_2O_3 (QReC, $\geq 99.5\%$) were mixed by planetary ball mill (PM, Restch PM 400) in ethanol for 12 h. The mixed power were calcined at 1273 K for 24 h in atmosphere and then hot pressed at 1173 K for 1 h under pressure 60 MPa in Argon atmosphere. The hot pressed pellets were annealed at 1473 K for 36 h in air. The pellets were pulverized to powder for analyzing crystal structure by X-ray diffraction (XRD, Shimadzu 6100) technique with Cu $K\alpha$ radiation, 2 deg/min of scan speed, 0.02 of sampling pitch and 20-80 degree of 2θ for scan ranges.

The Seebeck coefficient (S) and electrical resistivity (ρ) were measured by four point probe method with temperature ranges of 300 - 473 K in atmosphere. The S measurement followed by $-\Delta V/\Delta T$, where T is temperature and V is voltage. The ρ was measured from $\rho = RA/l$, where R is resistance, A is cross section area of material and l is probe distance. The thermal conductivity (κ) was measured by the steady-state method following the relation $\kappa = -\dot{Q}l/A\Delta T$, where \dot{Q} is heat rate.

In the case of Raman spectroscopy measurement, CMO was prepared following the standard sol-gel method. First, the stoichiometric reagents of $\text{Mn}(\text{NO}_3)_2 \cdot 4\text{H}_2\text{O}$ (Merck, $\geq 98.5\%$) and $\text{C}_6\text{H}_8\text{O}_7 \cdot \text{H}_2\text{O}$ (Merck, 99.5%) were separately dissolved in distilled water, while CaCO_3 (Sigma Aldrich, $\geq 99.0\%$) were dissolved in solutions composed of distilled water and HNO_3 (Pudak Scientific, 65%). Raman spectra were collected at room temperature using iHR 320 modular Raman (Horiba Jobin Yvon) spectrometer, equipped with a CCD detector and a solid-state laser source operating at 532 nm wavelength with appropriate filters. The spectrometer has spectral resolution of $1.22\text{ cm}^{-1}/\text{pixel}$, 600 gr/mm grating, and $100\times$ objective.

III. THEORETICAL METHODS

To obtain accurate geometry and electronic structure, we perform standard density-functional theory (DFT) calculations using the projected augmented wave (PAW) and spin-polarized bases, implemented in the QUANTUM ESPRESSO [21]. For the exchange-correlation function, we choose the revised generalized-gradient-approximation-Perdew-Burke-Ernzerhof (GGA-PBE) or the so-called the PBEsol functional [22], which is appropriate for a densely-packed solid surface. In the ground state, CMO is an antiferromagnetic (AFM) material [5] and it possesses a $Pnma$ space group containing 20 atoms in the unit cell (see Fig. 1). We apply $U = 5\text{ eV}$ on the DFT+U level to account for the localized Mn states according to a previous study by Molinari *et al.* [9]. The converged result is obtained by the sampling Brillouin zone with $2 \times 2 \times 2$ k -mesh and using a kinetic energy cutoff of 65 Ry. All atoms are relaxed until all forces are smaller than $1 \times 10^{-5}\text{ Ry/a.u.}$ The density of states (DOS) was obtained using the tetrahedron method [23]. We also perform calculations of phonon frequencies and eigenvectors of CMO at the Gamma point (zone center). The force constant is obtained from the density-functional perturbation theory (DFPT)+U [24]. Phonon frequencies and eigenvectors can be obtained from solving the dynamical matrix equation.

In order to understand the role of Bi doping into the electronic transport, we then calculate the electronic structure of BCMO. To make this model, we consider CMO $2 \times 2 \times 2$ supercell consisting of 160 atoms and replace one Ca atom in the center with one Bi atom, thus we have 3.125% doping. Having the electronic structures of CMO and BCMO, we can calculate thermoelectric properties such as Seebeck coefficient (S), electrical conductivity (σ), and electronic thermal conductivity (κ_e) within the linear Boltzmann transport theory and relaxation time approximation (τ) (RTA) as implemented in the BoltzTrap package [25]. The equations of S , σ , and κ are [12, 26, 27],

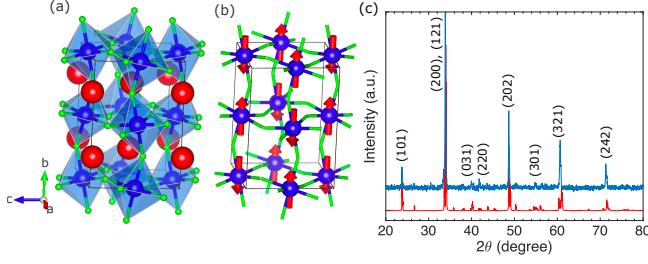


FIG. 1. (a) The geometrical structure of CMO. Ca atoms (red) are located at the center of orthorhombic lattice, Mn atoms (blue) are at the edges, Oxygens (green) surround Mn atoms making an octahedral structure. (b) CMO exhibits an anti-ferromagnetic ground state. (c) X-ray diffraction (XRD) pattern of CMO. Experimental XRD plot (blue line) is compared with theoretical XRD (red line).

$$S = -\frac{1}{qT} \frac{\sum_{i,\mathbf{k}} (E_{i\mathbf{k}} - \mu) v_{i\mathbf{k}}^2 \frac{\partial f_{i\mathbf{k}}}{\partial E_{i\mathbf{k}}}}{\sum_{i,\mathbf{k}} v_{i\mathbf{k}}^2 \frac{\partial f_{i\mathbf{k}}}{\partial E_{i\mathbf{k}}}}, \quad (1)$$

$$\sigma = -\frac{q^2}{NV} \sum_{i,\mathbf{k}} \tau v_{i\mathbf{k}}^2 \frac{\partial f_{i\mathbf{k}}}{\partial E_{i\mathbf{k}}}, \quad (2)$$

$$\kappa_e = \frac{1}{NV} \sum_{i,\mathbf{k}} -\frac{(E_{i\mathbf{k}} - \mu)^2}{T} v_{i\mathbf{k}}^2 \tau \frac{\partial f_{i\mathbf{k}}}{\partial E_{i\mathbf{k}}} - TS^2 \sigma, \quad (3)$$

where q is the carrier charge $\pm e$ for hole and electron, respectively, T is the average temperature of a material, N is the number of \mathbf{k} points in the Brillouin zone, V is the volume of unit cell, μ is the Fermi energy, $f_{i\mathbf{k}}$ is the Fermi-Dirac distribution, and $v_{i\mathbf{k}}$ is the component of electronic group velocity. We assume that the scattering rate τ^{-1} is proportional to temperature.

Phonon thermal conductivity is calculated using the Debye-Callaway model with relaxation time approximation expressed as:

$$\kappa_{ph} = \frac{k_B}{2\pi^2\nu} \left(\frac{k_B}{\hbar}\right)^3 T^3 \int_0^{\Theta_D/T} \tau_{ph}(x) \frac{x^4 e^x}{(e^x - 1)^2} dx, \quad (4)$$

where $x = \hbar\omega/k_B T$, k_B is the Boltzmann constant, ν is the effective sound velocity, \hbar is the reduced Plank constant, $\Theta_D = \hbar\omega_D/k_B$ is the Debye temperature with $\hbar\omega_D$ is the largest phonon energy of the system and τ_{ph} is the phonon relaxation time. In this model, we assume that the Umklapp scattering dominates over other scattering events and it takes the form of relaxation time as:

$$\tau_{ph}^{-1}(\omega) = \frac{\hbar\gamma^2}{Mv^2\Theta_D} \omega^2 T, \quad (5)$$

where γ is the Grüneisen parameter and M is the average atomic mass.

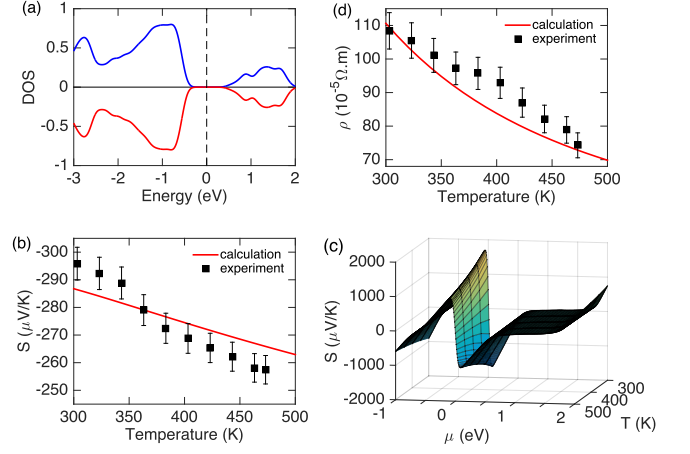


FIG. 2. Electronic structure and transport properties of pristine CMO. (a) The density of states of CMO. The blue line is for the spin-up and the red-line is for the spin-down components. (b) Experimental Seebeck coefficients S (dots) are compared with theoretical results (red line) for a chemical potential $\mu = 0.5$ eV. The y -axis is inverted to emphasize the absolute value of S while keeping the negative sign for n -type semiconductors. (c) Three-dimensional plot of theoretical S as a function of chemical potential μ and temperature T under relaxation time approximation. At small μ and T , the Seebeck coefficient can be optimized to reach ~ 1600 $\mu\text{V/K}$. (d) Experimental resistivity ρ (dots) compared with theoretical resistivity (red line) of Eq. (2). We have adopted $\tau^{-1} \propto T$ in the theoretical model.

IV. RESULTS AND DISCUSSION

A. CMO geometrical structure

In Figure 1(a), we show the orthorhombic perovskite unit cell of pristine CMO. Anti-ferromagnetic ordering from Mn sublattice refers to Goodenough [28] shown in Fig. 1(b). The relaxed structure is then compared with the XRD of CMO sample in Fig. 1(c). The blue line is the experimental results while the red line is obtained from DFT, which is in good agreement with the experiments. We obtain lattice constants $a = 5.3265\text{\AA}$, $b = 7.4319\text{\AA}$, and $c = 5.2523\text{\AA}$ with a discrepancy about 0.5% from the experimental results.

B. CMO electronic structure and transport

The electronic structure is calculated based on the relaxed structure. We obtain density of states in Fig. 2(a) for the spin-up (blue line) and spin-down (red line) cases. The anti-ferromagnetic insulator state is confirmed with a band gap of about 1 eV which reproduces previous optical spectroscopy results [29]. Calculated Seebeck coefficient obtained from Eq. (1) is shown in Fig. 2(b) compared with the experiments (dots). This fitting will give the Fermi energy $\mu = 0.5$ eV measured from the theoretical charge neutrality point (vertical dashed line) in

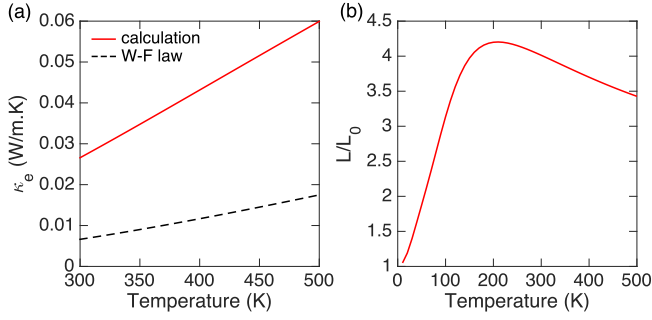


FIG. 3. (a) Electronic thermal conductivity κ_e of pristine CMO as a function of temperature obtained from Eq. (3) (solid red line) compared with the prediction from the Wiedemann-Franz law (black dashed line). (b) Calculated Lorenz number as a function of temperature in units of $L_0 = (\pi k_B/e)^2/3$.

Fig. 2(a). It means that the Fermi energy is located at the edge of the conduction band. The negative sign of the Seebeck coefficient indicates that the CMO is n-doped. Inverse proportionality of $|S|$ with respect to T indicates the semiconducting or insulating nature of CMO which contrasts with the metallic systems [12]. Theoretically, the Seebeck coefficient may be amplified by one order of magnitude if the Fermi energy is located near $\mu = 0$ as shown in Fig. 2(c). Such a high Seebeck coefficient has been achieved in organic perovskites and could be possible to achieve in perovskite oxides [30]. The sign change of S occurs due to the ambipolar effect following electron or hole charge as majority or minority carriers. Inverse proportionality of $|S|$ vs T persists in different μ .

We can further proceed to the determination of electrical resistivity $\rho = 1/\sigma$ from Eq. (2) and compare with the experimental results. In Fig. 2(d) we show ρ as a function of temperature. We obtain $\tau^{-1} = \alpha T + \beta$ with $\alpha = 0.008 \text{ fs}^{-1}\text{K}^{-1}$ and $\beta = 0.4 \text{ fs}^{-1}$. The τ^{-1} is proportional to temperature as expected in electron-phonon scattering, i.e., the number of phonon increases by thermal excitation. The decrease of ρ as a function of temperature is expected in semiconductors in which carrier concentration increases by thermal excitation.

We show the calculated electronic thermal conductivity κ_e from Eq. (3) in Fig. 3(a). One can compare the electron's efficacy to conduct heat versus current using the WF law, $\kappa_e = LT/\rho$, where L is the Lorenz number. For ordinary metals, we have $\kappa_e^{(0)} = L_0 T/\rho$, where $L_0 = (\pi k_B/e)^2/3$. Plugging in ρ from Fig. 2(d), we obtain $\kappa_e^{(0)}$ as the dashed line in Fig. 3(a). The κ_e value is typically about four times larger than the expected $\kappa_e^{(0)}$ from the WF law with temperature dependence as shown in Fig. 3(b). These results suggest that the localized electrons in Mn orbitals conduct heat more efficiently than the current, resulting in a drawback for TE application. Violation of the WF law has been reported in many strongly correlated systems [15–17] but suggested value of L/L_0 is less than unity. Although the relation-

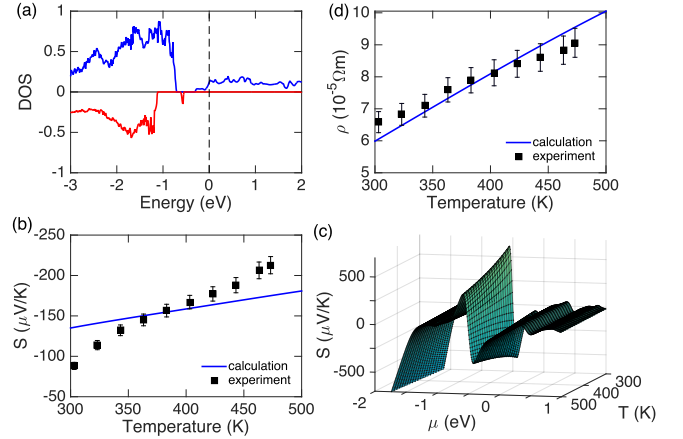


FIG. 4. Electronic structure and transport properties of BCMO. (a) The density of states of BCMO. The blue (red) line refers to spin-up (down) states. (b) The Seebeck coefficient as a function of temperature from Eq. 1 (blue line) and experimental results (dots). (c) The Seebeck coefficient as a function of the Fermi energy μ and temperature T .

ship of L with the strength of Coulomb interaction U is very instructive to study in detail to understand this phenomenon, the in-depth investigation will be presented elsewhere and not of main importance in this discussion as κ_e value is negligible compared with total κ in Fig. 7. As can be seen later in Fig. 5, Bi substitution on Ca site reduces L/L_0 ratio recovering the metallic nature.

C. BCMO electronic structure and transport

One way to improve thermoelectric properties of CMO is by performing atomic substitution of Bi to the Ca site. With this substitution, the two distinct ions, Mn^{3+} that sits next to Bi ion and Mn^{4+} in the proximity of Ca ions, will perform double exchange (DE) mechanism mediated by oxygen [3, 20]. This DE interaction delocalizes electrons in the Mn d orbitals and favors metal ferromagnetic ground state [20]. This can be seen in the density of states of BCMO in Fig. 4(a). The Fermi energy lies in the conduction band with an imbalanced spin-up population over the spin-down component. As a result, electronic transport properties would be expected to mimic metallic Fermi gas. Nevertheless, the strongly correlated nature remains, as can be seen in the reduced band gap ($\sim 0.5 \text{ eV}$) below the Fermi level owing to the on-site Coulomb interaction U .

In contrast to that of pristine CMO, the Seebeck coefficient of BCMO is proportional to temperature [cf. Fig. 4(b) and Fig. 2(b)], as expected from linear scaling in metal $|S| = \pi^2 k_B T / 2e\mu$ [12]. From this fitting, we obtain $\mu = -0.25 \text{ eV}$ which means that the Fermi energy is located at the edge of the conduction band. The optimum Seebeck coefficient is about $500 \mu\text{V/K}$ or about four times smaller than that of the pristine sample. This

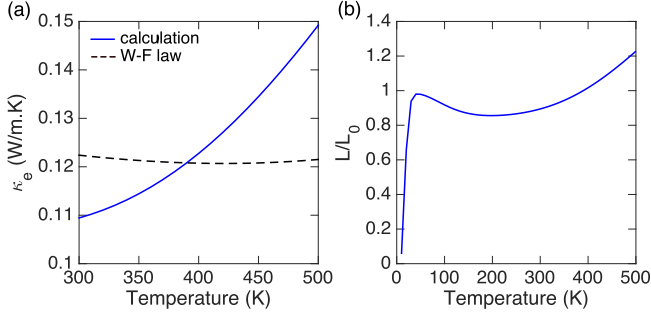


FIG. 5. (a) Electronic thermal conductivity κ_e of BCMO as a function of temperature from Eq. (3) (blue solid line) compared with the prediction from the Wiedemann-Franz law (black dashed line). (b) Calculated Lorenz number as a function of temperature compared with $L_0 = (\pi k_B/e)^2/3$.

optimum value can be achieved by positioning the Fermi energy μ at the band gap and at a small temperature as shown in Fig. 4(c).

Opposite behavior of CMO with respect to BCMO transport can also be seen from the resistivity ρ profile that increases proportional to T in Fig. 4(d). For a conventional metal with $\mu \gg k_B T$, electrical conductivity takes the form $\sigma = \rho^{-1} = \frac{e^2}{2\pi\hbar^2} \tau \mu$. Thus the only dependence of ρ on T comes from the temperature dependence of relaxation time (τ). Indeed, by taking the relaxation rate as $\tau^{-1} = \alpha T + \beta$, with $\alpha = 0.013 \text{ fs}^{-1}\text{K}^{-1}$ and $\beta = 0.2 \text{ fs}^{-1}$, the calculated resistivity reproduces the experimental results. We note parenthetically that scattering rate of BCMO is 1.5 times larger than that of CMO. In other words, electron lifetime in the BCMO is reduced due to Bi doping. Importantly, despite the reduction of electronic lifetime, the resistivity of BCMO decreases by one order of magnitude compared with the CMO, thanks to the metallic nature of the BCMO, hence resulting in a better TE performance.

The electronic thermal conductivity of BCMO is shown to be linearly proportional to temperature. However, this trend cannot be reproduced from the WF law [see Fig. 5(a)] because this system also possesses Lorenz number that depends on temperature [Fig. 5(b)]. Nevertheless, the L/L_0 ratio does not strongly depart from unity which signifies the contribution from Bi doping to recover the metallic character of CMO. In contrast to pristine CMO, L/L_0 can be less than unity at temperature below 380 K.

D. Phonons in CMO and BCMO

1. Raman Spectroscopy of CMO and BCMO

Raman spectroscopy offers a sensitive probe to determine the amount of bismuth-doped to the CMO. Experimental Raman spectra of CMO and BCMO are shown in Fig. 6 for unpolarized light. Short lines below the spec-

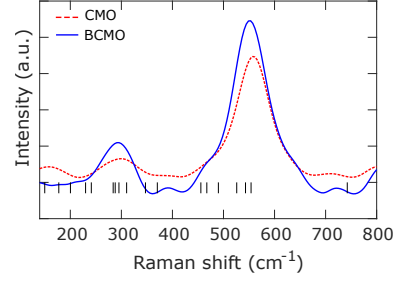


FIG. 6. Experimental Raman spectroscopy of pristine CMO (red dash line) and BCMO (blue solid line). Short vertical lines indicate the frequencies of theoretically Raman active modes in CMO.

tra are theoretical Raman active modes. The prominent peak at 557 cm^{-1} of pristine CMO is assigned to the A_g mode due to the in-phase stretching mode of MnO_6 bi-octahedral [4, 6]. The presence of Bi doping red-shifts this peak to become 549 cm^{-1} because the average mass increases. Apart from the peak shifts, the Raman spectral linewidth also broadens indicating shorter phonon lifetime due to the increase of anharmonicity. This information will be useful to characterize thermal conductivity in the next section.

2. Phonon contribution to thermal conductivity

Using the simplified Callaway-Debye model in Eq. 4 and assuming that the Umklapp scattering is dominant, we can reproduce the measured thermal conductivity of pristine CMO as shown in Fig. 7(a). For pristine CMO, we use the Debye temperature 800 K assuming that the phonon 557 cm^{-1} observed in Raman spectra as the Debye frequency and the Grüneisen parameter $\gamma = 3.45$ from the previous work [31]. We obtain effective sound velocity $\nu = 1.38 \text{ km/s}$ which is typically comparable to the similar work by Israel group [8]. For BCMO, we use the Debye temperature 790 K corresponding to the red-shifted Raman peak 549 cm^{-1} and Grüneisen parameter $\gamma = 3.47$ to obtain $\nu = 0.81 \text{ km/s}$.

It is important to note that Bi doping decreases thermal conductivity and electronic resistivity. The decrease of resistivity by 10 times can overcome the decrease of the Seebeck coefficient by 2 times that makes BCMO power factor, $PF = S^2/\rho$ stays superior compared with pristine CMO as shown in Fig. 7(b). We show in this figure, the power factor of BCMO may, in principle, be amplified up to four times compared to the experiment if the Fermi energy is located near $\mu = 1.7 \text{ eV}$. The dimensionless figure of merit, $ZT = S^2 T / \rho \kappa$ in Fig. 7(c) shows that the thermoelectric performance in CMO can be improved by Bi doping.

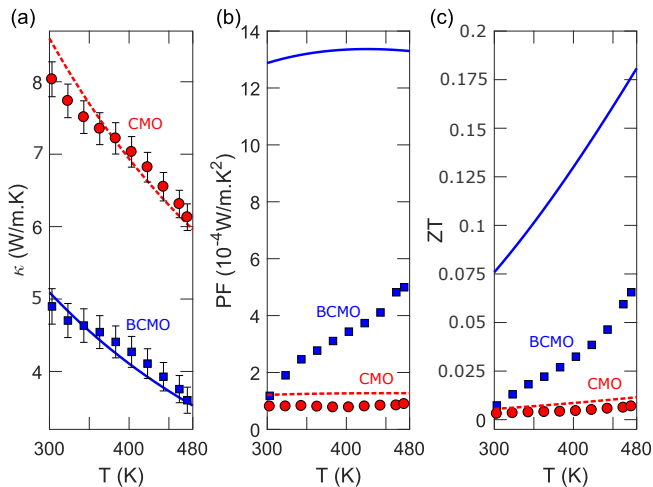


FIG. 7. Thermoelectric properties of CMO and BCMO. The experimental (theoretical) results are denoted by symbols (lines). Red circles and dashed lines are for CMO, while blue squares and solid lines are for BCMO. Panel (a) shows experimental thermal conductivity κ and theoretical phonon thermal conductivity κ_{ph} from Eq. (4). Electronic thermal conductivity can be neglected in the fitting because its values are about two orders of magnitude smaller than κ_{ph} . In panels (b) and (c), respectively, the measured power factor and dimensionless figure of merit are compared with the optimized values from theoretical prediction.

V. CONCLUSIONS

We have characterized the electronic and phonon properties of CMO and BCMO via thermoelectric transport measurements and first principles calculations. CMO has anti-ferromagnet insulator ground states thus having large Seebeck coefficient and resistivity. The strongly correlated nature of CMO manifests in the breakdown of WF law in which the Lorenz number reaching four times larger than that of ordinary metals. Upon Bi-doping, the resistivity decreases by ten times and the Seebeck coefficient decreases by two times giving a larger power factor than the pristine one. BCMO also recovers the obedience to WF law. The presence of Bi doping also lowers down the sound velocity as well as phonon lifetime as confirmed by the Raman spectroscopy. Overall, Bi doping enhances the TE figure of merit because of improvement in electronic transport and degradation in phonon thermal transport.

ACKNOWLEDGMENTS

This research was partially funded by a collaboration grant from Sestama-LIPI for a visit to Thailand and by a research grant from Indonesia Toray Science Foundation. M.N. acknowledges a research grant from Brawijaya University No. 3/UN10.F09/PN/2019. W.B.K.P. acknowledges Raman research facilities in LIPI Research Center for Physics. TS and KS acknowledge TRF Research Career Development Grant RSA6180070.

-
- [1] G. H. Jonker and J. H. van Santen, “Ferromagnetic compounds of manganese with perovskite structure,” *Physica* **16**, 337–349 (1950).
 - [2] J. H. van Santen and G. H. Jonker, “Electrical conductivity of ferromagnetic compounds of manganese with perovskite structure,” *Physica* **16**, 599–600 (1950).
 - [3] C. Zener, “Interaction between the d-shells in the transition metals. II. ferromagnetic compounds of manganese with perovskite structure,” *Phys. Rev.* **82**, 403 (1951).
 - [4] M. V. Abrashev, J. Bäckström, L. Börjesson, V. N. Popov, R. A. Chakalov, N. Kolev, R.-L. Meng, and M. N. Iliev, “Raman spectroscopy of CaMnO_3 : mode assignment and relationship between raman line intensities and structural distortions,” *Phys. Rev. B* **65**, 184301 (2002).
 - [5] E. O. Wollan and W. C. Koehler, “Neutron diffraction study of the magnetic properties of the series of perovskite-type compounds $[(1-x)\text{La}, x\text{Ca}]\text{MnO}_3$,” *Phys. Rev.* **100**, 545–563 (1955).
 - [6] M. N. Iliev, M. V. Abrashev, H.-G. Lee, V. N. Popov, Y. Y. Sun, C. Thomsen, R. L. Meng, and C. W. Chu, “Raman spectroscopy of orthorhombic perovskite-like YMnO_3 and LaMnO_3 ,” *Phys. Rev. B* **57**, 2872 (1998).
 - [7] J. G. Bednorz and K. A. Miller, “Perovskite-type oxides—The new approach to high- T_c superconductivity,” *Rev. Mod. Phys.* **60**, 585 (1988).
 - [8] A. Baranovskiy, A. Graff, J. Klose, J. Mayer, and Y. Amouyal, “On the origin of vibrational properties of calcium manganate based thermoelectric compounds,” *Nano Energy* **47**, 451–462 (2018).
 - [9] M. Molinari, D. A. Tompsett, S. C. Parker, F. Azough, and R. Freer, “Structural, electronic and thermoelectric behaviour of CaMnO_3 and $\text{CaMnO}_{(3-\delta)}$,” *J. Mater. Chem. A* **2**, 14109–14117 (2014).
 - [10] T. Seetawan, K. Singsoog, S. Srichai, C. Thanachayanont, V. Amornkitbamrung, and P. Chindapasirt, “Thermoelectric energy conversion of p- $\text{Ca}_3\text{Co}_4\text{O}_9$ /n- CaMnO_3 module,” *Energy Procedia* **61**, 1067–1070 (2014).
 - [11] S. Paengson, P. Pilasuta, K. Singsoog, W. Namhongsa, W. Impho, and T. Seetawan, “Improvement in thermoelectric properties of CaMnO_3 by bi doping and hot pressing,” *Mater. Today-Proc.* **4**, 6289–6295 (2017).
 - [12] H. J. Goldsmid, *Introduction to thermoelectricity*, Vol. 121 (Springer, 2010).
 - [13] M. Zebajadi, K. Esfarjani, M.S. Dresselhaus, Z.F. Ren, and G. Chen, “Perspectives on thermoelectrics: from fundamentals to device applications,” *Energ. Environ. Sci.*

- 5**, 5147–5162 (2012).
- [14] R. Franz and G. Wiedemann, “Ueber die wärmeleitfähigkeit der metalle,” *Ann. Phys.* **165**, 497–531 (1853).
 - [15] R. Mahajan, M. Barkeshli, and S. A. Hartnoll, “Non-fermi liquids and the wiedemann-franz law,” *Phys. Rev. B* **88**, 125107 (2013).
 - [16] A. Principi and G. Vignale, “Violation of the wiedemann-franz law in hydrodynamic electron liquids,” *Phys. Rev. Lett.* **115**, 056603 (2015).
 - [17] A. Lavasani, D. Bulmash, and S. D. Sarma, “Wiedemann-franz law and fermi liquids,” *Phys. Rev. B* **99**, 085104 (2019).
 - [18] Y.-H. Lin, J. Lan, and C. Nan, *Oxide Thermoelectric Materials* (Wiley-VCH, 2019).
 - [19] U. Aschauer, R. Pfenninger, S. M. Selbach, T. Grande, and N. A. Spaldin, “Strain-controlled oxygen vacancy formation and ordering in CaMnO_3 ,” *Phys. Rev. B* **88**, 054111 (2013).
 - [20] P. W. Anderson and H. Hasegawa, “Considerations on double exchange,” *Phys. Rev.* **100**, 675–681 (1955).
 - [21] P. Giannozzi, S. Baroni, N. Bonini, M. Calandra, R. Car, C. Cavazzoni, D. Ceresoli, G. L. Chiarotti, M. Cococcioni, I. Dabo, *et al.*, “QUANTUM ESPRESSO: a modular and open-source software project for quantum simulations of materials,” *J. Phys. Condens. Matter* **21**, 395502 (2009).
 - [22] J. P. Perdew, A. Ruzsinszky, G. I. Csonka, O. A. Vydrov, G. E. Scuseria, L. A. Constantin, X. Zhou, and K. Burke, “Restoring the density-gradient expansion for exchange in solids and surfaces,” *Phys. Rev. Lett.* **100**, 136406 (2008).
 - [23] P. E. Blöchl, O. Jepsen, and O. K. Andersen, “Improved tetrahedron method for brillouin-zone integrations,” *Phys. Rev. B* **49**, 16223–16233 (1994).
 - [24] M. Cococcioni and S. de Gironcoli, “Linear response approach to the calculation of the effective interaction parameters in the LDA + U method,” *Phys. Rev. B* **71**, 035105 (2005).
 - [25] G. K. H. Madsen and D. J. Singh, “Boltztrap. a code for calculating band-structure dependent quantities,” *Comput. Phys. Commun.* **175**, 67–71 (2006).
 - [26] B. Liao, J. Zhou, B. Qiu, M. S. Dresselhaus, and G. Chen, “Ab initio study of electron-phonon interaction in phosphorene,” *Phys. Rev. B* **91**, 235419 (2015).
 - [27] W. Li, “Electrical transport limited by electron-phonon coupling from boltzmann transport equation: An ab initio study of Si, Al, and MoS_2 ,” *Phys. Rev. B* **92**, 075405 (2015).
 - [28] J. B. Goodenough, “Theory of the role of covalence in the perovskite-type manganites $[\text{La}, \text{M}(\text{II})]\text{MnO}_3$,” *Phys. Rev.* **100**, 564 (1955).
 - [29] J. Jung, K. Kim, D. Eom, T. Noh, and E. Choi, “Determination of electronic band structures of and using optical-conductivity analyses,” *Phys. Rev. B* **55**, 15489 (1997).
 - [30] T. Ye, X. Wang, X. Li, A. Q. Yan, S. Ramakrishna, and J. Xu, “Ultra-high Seebeck coefficient and low thermal conductivity of a centimeter-sized perovskite single crystal acquired by a modified fast growth method,” *J. Mater. Chem. C* **5**, 1255–1260 (2017).
 - [31] A. Srivastava and N. K. Gaur, “Bulk modulus and thermodynamic properties of electron-doped calcium manganate- $\text{Ca}_{1-x}\text{RE}_x\text{MnO}_3$,” *J. Magn. Magn. Mater.* **321**, 3854–3865 (2009).